ACS APPLIED MATERIALS & INTERFACES

Research Article

www.acsami.org

Lutecium Fluoride Hollow Mesoporous Spheres with Enhanced Up-Conversion Luminescent Bioimaging and Light-Triggered Drug Release by Gold Nanocrystals

Ruichan Lv,[†] Piaoping Yang,*[,†] Yunlu Dai,[†] Shili Gai,[†] Fei He,[†] and Jun Lin*[,‡]

[†]Key Laboratory of Superlight Materials and Surface Technology, Ministry of Education, Harbin Engineering University, Harbin 150001, P. R. China

[‡]State Key Laboratory of Rare Earth Resource Utilization, Changchun Institute of Applied Chemistry, Chinese Academy of Sciences, Changchun 130021, P. R. China

Supporting Information

ABSTRACT: Uniform $Na_5Lu_9F_{32}$ hollow mesoporous spheres (HMSs) have been successfully prepared by a facile and mild (50 °C for 5 h) coprecipitation process, and Au nanocrystals (NCs) with particle size of about 10 nm were conjugated to poly(ether imide) (PEI) modified HMSs by electrostatic interaction. Compared with $Na_5Lu_9F_{32}$:Yb/Er HMSs, the up-conversion (UC) luminescence intensity of $Na_5Lu_9F_{32}$:Yb/Er@Au HMSs was much higher under low pump power due to the local field enhancement (LFE) of Au NCs, and there is a surface plasmon resonance (SPR) effect with nonradiative transitions which generates a thermal effect. These two effects have been proved by theoretical discrete-dipole approximation (DDA) simulation. The good biocompatibility of $Na_5Lu_9F_{32}$:Yb/Er@Au HMSs indicates them as a promising candidate in the biological field. Particularly, under near-infrared (NIR) laser irradiation, a rapid doxorubicin (DOX) release was achieved due to the thermal effect of Au NCs. In this case, $Na_5Lu_9F_{32}$:Yb/Er@Au HMSs exhibit an apparent NIR light-controlled "on/off" drug release pattern. In addition, UC luminescent images uptaken by cells show brighter green and red emission under NIR laser excitation. Therefore, this novel multifunctional (mesoporous, enhanced UC luminescent, and light-triggered drug release) material should be potential as a suitable targeted cancer therapy carrier and bioimaging.

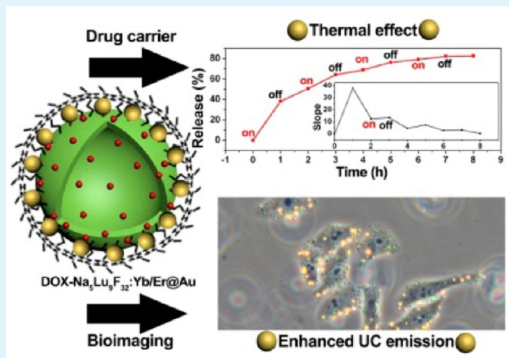

KEYWORDS: *hollow, mesoporous, up-conversion luminescence, light-triggered*

■ INTRODUCTION

Drug delivery systems (DDSs) have been widely researched because the rapid release and large dosage of conventional pharmaceuticals could cause severe side effects to normal tissues.[1] The key ability of DDSs was to regulate the drug release process, minimize side effects, and improve therapeutic efficacy.[2] Meanwhile, in the field of DDSs, hollow mesoporous spheres (HMSs) have gained special attention because they simultaneously have large voids and mesoporous shells.[3−6] The large voids make it possible to store more drug molecules than the conventional materials, and the mesoporous shells can provide accessible channels for drug molecule diffusion and mass transfer which could make drug molecules release modestly. Additionally, endogenous and exogenous activation are two approaches which can be used to control the release of the therapeutic payload from the carrier. A further strategy for creating enhanced DDSs is the activation of therapeutics at the desired site to provide spatiotemporal localization of treatment.[7] Therefore, it is meaningful to find activations which could provide a highly orthogonal external stimulus, allowing spatiotemporal control of payload release.[8,9]

Up-conversion nanocrystals (UCNs) which can efficiently convert near-infrared (NIR) reflection from inexpensive diode lasers into visible light by multiphoton absorption are the particular potential material for drug carrier and bioimaging because the use of NIR excitation virtually eliminates the unwanted fluorescence background signal;[10−17] meanwhile, NIR has deep tissue penetration and is safe to biological cells.[18−22] If UCNs are utilized in the DDSs, the UC luminescent images uptaken by cells would be advantageous to the target tracking treatment which has the multifunctional bioimaging. Therefore, Ln-codoped (Ln = Yb/Er, Yb/Ho, and Yb/Tm) rare earth fluoride with hollow porous structure has attracted wide interest due to the low vibrational energy and outstanding thermal and environmental stability, all of which result in the minimization of quenching concentration of the excited rare earth ions and wide application as luminescent material.[23−32] However, as a kind of surface defect, the hollow

Received: July 4, 2014
Accepted: August 20, 2014
Published: August 20, 2014

dx.doi.org/10.1021/am504347e | ACS Appl. Mater. Interfaces 2014, 6, 15550−15563

structure is not good for the emission intensity and the luminescent efficiency. Scientists have proposed different methods to adjust the luminescent property.[33,34] Plasmonic modulation is an effective way to change the luminescence by virtue of surface plasmon resonance (SPR) or local field enhancement (LFE) effect.[35−38] The LFE effect increases the excitation of the fluorescent ions which enhance the luminescence, while the SPR effect is affected by the near-field electrodynamical environment which can cause a quenching of the UC relative to the native state.[39]

The discrete-dipole approximation (DDA) simulation, which works by simulating nanocrystals as a defined array of polarizable points, is a flexible method for computing the absorption and scattering components of the extinction.[40,41] Through the theoretical calculation, LFE strength and the SPR peaks of the material could be evaluated accurately. Up to now, though, there are many reports that proposed the SPR effect from UCNs and Au NCs for optical enhancement,[42−44] and few reports are concerned with the nonradiative energy transfer which may produce a thermal effect as an effective controllable tool to regulate the release efficiency.[45]

Herein, we synthesized $Na_5Lu_9F_{32}$:Yb/Er hollow mesoporous microspheres using the facile large-scale coprecipitation method. When the lanthanide fluoride HMSs were modified by poly(ether imide) (PEI), Au NCs with the average size of about 10 nm were conjugated. UC luminescent properties (including the emission intensity with different pump powers, lifetimes, and nonradiation properties), DDA simulation, MTT assay, DOX release, and UC luminescence imaging properties of $Na_5Lu_9F_{32}$:Yb/Er HMSs and $Na_5Lu_9F_{32}$:Yb/Er@Au HMSs were employed to evaluate the feasibility of this functional composite. In this study, as the final multifunctional material, $Na_5Lu_9F_{32}$:Yb/Er@Au HMSs have two obvious advantages compared with the conventional materials. First, UC luminescent intensity was enhanced under low pump power due to the LFE effect of Au NCs. Consequently, UC luminescent images uptaken by cells shows much brighter green and red emission under NIR laser excitation. Second, there is a surface plasmon resonance (SPR) effect which decreases green and red emissions but generates a thermal effect. By virtue of this thermal effect, under NIR laser irradiation, a rapid doxorubicin (DOX) release was achieved, and then $Na_5Lu_9F_{32}$:Yb/Er@Au HMSs exhibit an apparent light-controlled "on−off" drug release pattern. This novel multifunctional (mesoporous, enhanced UC luminescence, and light-triggered drug release) material should be potential as a suitable candidate for targeted cancer therapy carriers and bioimaging.

■ EXPERIMENTAL SECTION

Chemicals and Materials. All the chemical reagents used in this experiment are of analytical grade without any further purification, including urea, sodium fluoroborate ($NaBF_4$), sodium citrate, tannic acid, chloroauric acid ($HAuCl_4$) (from Beijing Chemical Corporation), Lu_2O_3 (99.99%), Yb_2O_3 (99.99%), Er_2O_3, Ho_2O_3, and Tm_2O_3 (99.99%) (from Sinopharm Chemical Reagent Co., Ltd.), poly(ether imide) (PEI), DOX, phosphate-buffered saline (PBS), and potassium hydrogen phthalate (PHP) (Tianjin Kermel Chemical Reagent Co., Ltd.)

Synthesis of the Precursors. The well-dispersed precursors were prepared via a precipitation process according to a published report with some modification.[46] In a typical process, 0.5 M $Ln(NO_3)_3$ was prepared by dissolving calculated Ln_2O_3 into HNO_3 with gradual heating. A total of 1 mL of 0.5 M $Ln(NO_3)_3$ and 1.5 g of urea were dissolved in 50 mL of deionized water in a beaker. After continuous stirring for 10 min, heating of the mixture was continued at 90 °C for 2 h through a water bath. The resulting mixture was centrifuged at 6000 rpm for 4 min, and the washing process was repeated three times.

Synthesis of $Na_5Lu_9F_{32}$ HMSs. The as-prepared precursor was dissolved by 10 mL of deionized water, and then 0.44 g of $NaBF_4$ was added with continuous stirring. After the solution appeared uniform, the beaker was transferred to the water bath kettle at 50 °C. After reacting for 5 h, the resulting product was washed three times and dried for 12 h to obtain $Na_5Lu_9F_{32}$:15%Yb,1%Er (Tm, Ho) HMSs.

Preparation of $Na_5Lu_9F_{32}$:Yb/Er@Au. The Au nanocrystals with a diameter of about 10 nm were prepared by the citrate reduction method in the presence of tannic acid as reducing agent. Typically, 5 mL of 1 g/L $HAuCl_4$ was mixed with 30 mL of deionized water containing 0.2 g of sodium citrate and 0.03 g of tannic acid and kept at 60 °C for 4 h. Then, the as-prepared $Na_5Lu_9F_{32}$:Yb/Er HMSs were dispersed in 20 mL of water containing 0.1 g of PEI and stirred for 2 h. The PEI modified $Na_5Lu_9F_{32}$:Yb/Er HMSs were collected by centrifugation, washed by deionized water, and redispersed in 20 mL of deionized water. Consequently, 1 mL of the as-prepared gold suspension was swiftly added into the above solution and slowly rotated for 2 h, and the $Na_5Lu_9F_{32}$:Yb/Er@Au microspheres were collected by centrifugation.

In Vitro Viability of $Na_5Lu_9F_{32}$:Yb/Er@Au. A 5 mg/mL 3-[4,5-dimethylthiazol-2-yl]-2,5-diphenyl tetrazolium bromide (MTT) solution was prepared by using PBS as solvent. An amount of 200 mL of material per well plated with 5000−6000 L929 fibroblast cells was put in a 96-well plate. For blank control, there were 8 wells of cells incubated in the culture medium alone and then incubated 24 h in order to make the cells attach to wells with 5% CO_2 at 37 °C. $Na_5Lu_9F_{32}$:Yb/Er@Au HMSs were sterilized via UV irradiation for 2 h. After that, they were diluted into respective concentrations of 7.8125, 15.625, 31.25, 62.5, 125, and 250 μg/mL, and then the solutions were added to the wells and incubated for another 24 h at 37 °C with 5% CO_2. An amount of 20 μL of the prepared MTT solution was added to each well with different amount. The plate was subsequently incubated for another 4 h at 37 °C. Meanwhile, viable cells make MTT reduce into formazan which can be dissolved by dimethyl sulfoxide. After that, 150 μL of dimethyl sulfoxide was added to each well and placed on a shaking table for 5 min of 150 rpm in order to blend the formazan and solvent completely. The following formula was used to calculate cell viability: cell viability (%) = (mean of abs. value of treatment group/mean of abs. value of control) × 100%.

Hemolysis Assay. Through removing the serum from the EDTA.K2 stabilized human blood and washing with 1% normal saline with centrifugation, we have obtained the red blood cells for the next step. The red cells were diluted to 1/10 with PBS solution (pH = 7.4). Diluted cell suspension (0.3 mL) was then mixed with (1) PBS (1.2 mL) as a negative control; (2) deionized water (1.2 mL) as a positive control; and (3) the materials suspensions (1.2 mL) with varying concentrations (7.81, 15.63, 31.25, 62.5, 125, and 250 μg/mL). The eight samples kept stable for 2 h and then centrifuged at 4000 rpm for 4 min. The absorbance of the upper supernatants was measured by UV−vis characterization. The percentage of hemolysis was calculated using the equation: hemolysis % = $(A_{sample} - A_{(-)})/(A_{(+)} - A_{(-)})$, where A is the absorbance of the samples.

DOX Loading and Release Test. An amount of 0.03 g of $Na_5Lu_9F_{32}$:Yb/Er@Au HMSs was added into 5 mL of PBS and ultrasonic dispersed. After that, 0.0025 g of DOX was added into the solution with slow stirring at room temperature for 24 h. The as-prepared mixture was centrifugally separated at 6000 rpm for 4 min, and then the supernatant solution was kept for ultraviolet visible (UV) analysis. An amount of 10 mL of fresh PBS was replenished in the centrifugal tube and set in the water bath kettle at 37 °C with magnetic stirring for 10 min, and the supernatant solution was kept. The process was repeated with a changed release time as 1, 2, 3, 4, 5, 8, 12, 24, and 32 h, respectively. The two compared groups were proceeding with and without 980 nm irradiation. PBS (pH = 7) and PHP (pH = 4) were prepared directly by a pH modifier. The loading amount and concentration of DOX in the solution were determined by UV−vis measurement. Figure S1 (Supporting Information) shows the absorption spectrum between 350 and 600 nm, and the peak at 480 nm is used as the typical absorbance of the estimated solution. The relationship between the absorbance at 480 nm and the concentration of standard DOX solution is given in the inset of Figure S1 (Supporting Information). Through testing the absorbance of the supermatant at 480 nm with different release time, the mass of released DOX was obtained by the conversion of the absorbance to concentration with multiplied volume. The loading amount (M_{LA}) can be calculated using the formula $M_{LA} = O_{DOX} - R_{DOX}$, where O_{DOX} is the original DOX concentration and R_{DOX} is the residual concentration. The loading efficiency (LE %) can be calculated using the formula: LE = M_{LA}/O_{DOX}. The release efficiency (RE %) can be calculated using the formula RE = $\Sigma\, M_{DOXinsupermatant}/M_{LA}$, where $M_{DOXinsupermatant}$ is the DOX concentration in the supernatant with different release time.

In Vitro Cytotoxicity of $Na_5Lu_9F_{32}$:Yb/Er@Au. HeLa cells were plated out in 96-well plates at a density of 8000 cells per well and grew overnight to make cells attached. $Na_5Lu_9F_{32}$:Yb/Er@Au, DOX-$Na_5Lu_9F_{32}$:Yb/Er@Au, and DOX were added to the medium, and the cells were incubated in 5% CO_2 at 37 °C for 24 h. The concentrations of DOX were regulated to 0.78, 1.56, 3.13, 6.25, 12.5, and 25 μg/mL. The concentrations of $Na_5Lu_9F_{32}$:Yb/Er@Au and DOX-$Na_5Lu_9F_{32}$:Yb/Er@Au were regulated to 15.6, 31.3, 62.5, 125, and 250 μg/mL. The NIR irradiation was carried out when the incubation time was 5 h and irradiation was continued for 5 min with the pump power of 0.6 W/cm^2. At the end of the incubation process, 20 μL of MTT solution was added into each cell and incubated for another 4 h. The supernatant in each well was aspirated, and 150 μL of DMSO was added before the plate was examined using a microplate reader (Therom Multiskan MK3) at the wavelength of 490 nm.

UC Luminescence Microscopy (UCLM) Observation. The HeLa cells used for UC luminescence imaging were seeded in 6-well culture plates (5 × 10^4/well) and then incubated overnight as a monolayer. After that, these cells were incubated for different times (1 and 6 h) at 37 °C with 1 mL of 1 mg/mL $Na_5Lu_9F_{32}$:Yb/Er@Au HMSs. After incubation with different times, the cells were washed with PBS solution 3 times and fixed with 1 mL of 2.5% formaldehyde in each well for 10 min at 37 °C. After that, the as-prepared cells were washed with PBS three times in order to remove the attached HMSs.

Cellular Uptake. Cellular uptake by HeLa cancer cells was examined using a confocal laser scanning microscope (CLSM). The HeLa cells were seeded in a 6-well culture plate (a clean coverslip was put in each well) and grown overnight as a monolayer. Then, they were incubated with as-prepared $Na_5Lu_9F_{32}$:Yb/Er@Au + DOX at 37 °C for 30 min, 3 h, and 6 h, respectively. After that, the cells were rinsed with PBS three times, fixed with 2.5% formaldehyde (1 mL/well) at 37 °C for 10 min, and then rinsed with PBS three times again. In order to perform nucleus labeling, the nuclei were stained with DAPI solution (20 μg/mL in PBS, 1 mL/well) for 10 min. Then, the cells were rinsed with PBS three times. The coverslips were placed on a glass microscope slide, and the samples were visualized using CLSM (Leica TCS SP8).

DDA Calculations. In this work, the DDA starts by dividing the object of interest into a cubic array of N-point dipoles. Optical constants for Au and the refractive index dispersion of Au spheres with different wavelengths were used. A spherical target is subdivided with an array of cubic cells. After the interaction was solved iteratively between polarizable point dipoles in the cells and the incident light with different wavelengths, the cross sections for extinction and scattering could be generated. When there is more than one Au sphere, the effective radius was calculated as $a_{eff} \equiv (3V/4\pi)^{1/3}$, where V is the volume of the target. We have looked into the visible-near-infrared region (400−1200 nm). DDA is converged to a percent when the number of dipoles is larger than 10^3 with 1000 dipoles nm^{-3} in order to ensure accuracy.

Characterization. Powder X-ray diffraction (XRD) measurements were performed on a Rigaku D/max TTR-III diffractometer at a scanning rate of 15° per min in the 2θ range from 20° to 80°, with graphite monochromatized Cu Kα radiation (λ = 0.15405 nm). Images were obtained digitally on a scanning electron microscope (SEM, JSM-6480A), transmission electron microscope (TEM, FEI Tecnai G^2 S-Twin), and high-resolution transmission electron microscope (HRTEM). N_2 adsorption/desorption isotherms were obtained on a Micromeritics Tristar 3020 apparatus. Pore-size distribution was calculated from the adsorption branch of the N_2 adsorption/desorption isotherm and the Barrete Jonere Halenda method. UC emission spectra were acquired using a 980 nm laser diode (LD) Module (K98D08M-30W, China) as the irradiation source and detected by R955 (HAMAMATSU) from 400 to 800 nm. The spectra were detected after irradiation with the highest pump power for 5 min. DOX concentration was detected by a UV-1601 UV−vis spectrophotometer. Fourier transform infrared spectroscopy (FT-IR) spectra were measured on a PerkinElmer 580B IR spectrophotometer using the KBr pellet technique. The instrument of UCLM was rebuilt on an inverted fluorescence microscope (Nikon TieS), and an external CW 980 nm diode laser was illuminated. The measurements above were wholly performed at room temperature.

RESULTS AND DISCUSSION

Phase and Morphology Properties. Figure 1A shows the XRD patterns of $Na_5Lu_9F_{32}$:Yb/Er HMSs prepared at different reaction time. It is found that the product does not show obvious diffraction peaks after reacting for 0.5 h, indicating the noncrystalline nature. With the increase of reaction time, the crystalline fluorides gradually generate. When the time is 5 h, the diffractions of the as-obtained sample can be well indexed to cubic $Na_5Lu_9F_{32}$ (JCPDS No. 27-0725), indicating the high crystallinity of the sample. The EDS pattern of the sample (Figure 1B) reveals the presence of elements Na, Lu, Yb, and F

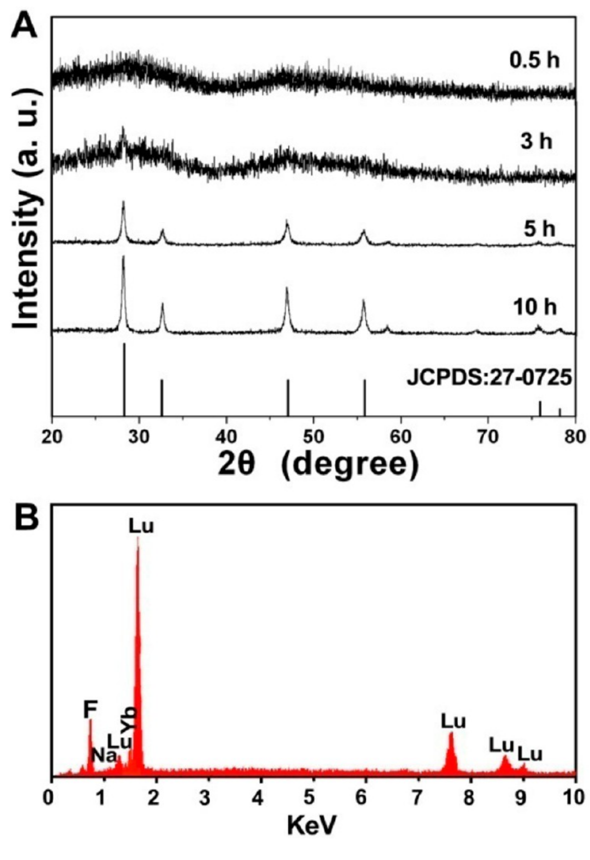

Figure 1. (A) XRD patterns of $Na_5Lu_9F_{32}$:Yb/Er obtained at the reaction time of 0.5−10 h and (B) the EDS pattern of $Na_5Lu_9F_{32}$:Yb/Er prepared at the reaction time of 5 h.

in the product. No C element is detected, confirming the complete conversion from $Lu(OH)CO_3$:Yb/Er to $Na_5Lu_9F_{32}$:Yb/Er. It is noted that the Er element cannot be found due to the low concentration.

Figure S2 (Supporting Information) gives the SEM images of the $Na_5Lu_9F_{32}$:Yb/Er precursor (S2A-B), and it is found that the precursor is well dispersed and has an average particle size of 180 nm. Figure 2A shows that the as-prepared

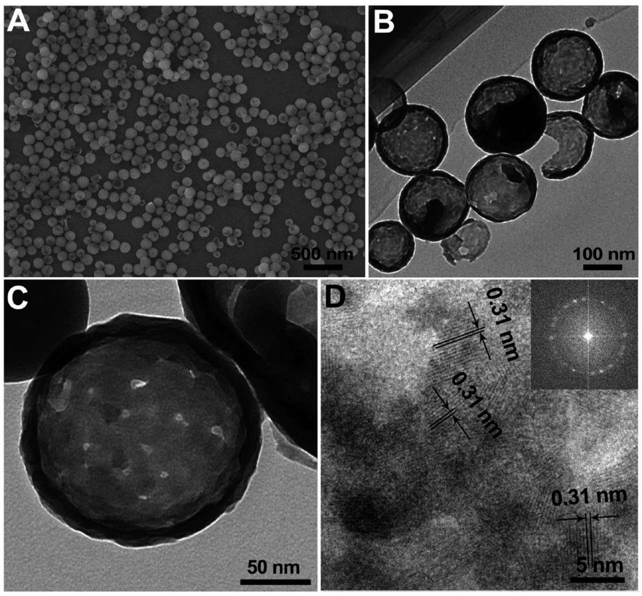

Figure 2. (A) SEM image, (B, C) TEM images with different magnification, and (D) HRTEM image of $Na_5Lu_9F_{32}$:Yb/Er HMSs.

$Na_5Lu_9F_{32}$:Yb/Er is uniform with an average diameter of 160−180 nm, and the broken pores reveal the hollow structure of the $Na_5Lu_9F_{32}$:Yb/Er. From the TEM images with different magnifications (Figure 2B−C), we can clearly see the strong contrast between the darker shell and brighter inside, further indicating the hollow structure of the product. In addition, there are obvious pores in the center of the hollow spheres, and the thickness of the shell is 10−20 nm. Figure 2D represents the apparent lattice fringes, and the dispersed lattice fringes further prove the pores inside. The interplanar distance between the adjacent fringes is calculated to be 0.31 nm, which can exactly be in conformity with the (111) plane spacing of cubic $Na_5Lu_9F_{32}$. The corresponding Fast Fourier transform pattern (inset in Figure 2D) shows the diffraction spots of the (111) planes of $Na_5Lu_9F_{32}$ and reveals the single-crystalline nature of the sample. The TEM results of $Na_5Lu_9F_{32}$:Yb/Er prepared at different reaction time (shown in Figure S3, Supporting Information) correspond well to the XRD result (Figure 1A). The formation mechanism of hollow spheres can be attributed to the Kirkendall effect.[47] During the fluorination, H^+, Na^+, and F^- ions are derived from the hydrolysis of $NaBF_4$, while the OH^- and CO_3^{2-} ions can be obtained from the precursor. After that, Na^+, Lu^{3+}, Ln^{3+}, and F^- ions precipitate to $Na_5Lu_9F_{32}$:Yb/Er, and the OH^- and CO_3^{2-} ions dissolve into the solution. Moreover, the large voids are generated because the dissolution rate is higher than the precipitation rate. As demonstrated in Figure S3B (Supporting Information), few irregular pores appear on the surface of the spheres after fluorination of 0.5 h. With the reaction proceeding, the H^+ ions dissolve and F^- ions precipitate with the residual precursor, and the $Na_5Lu_9F_{32}$:Yb/Er shell is formed gradually. As the reaction time is increased to 3 h (Figure S3C, Supporting Information), there are more pores formed with only a few surviving precursor particles inside. When the reaction time is up to 5 h, the hollow spheres are acquired without any precursor inside (Figure 2).

The positively charged PEI could strongly coordinate with the negatively charged gold nanocrystals; thus, before attaching with Au NCs, the surface of $Na_5Lu_9F_{32}$:Yb/Er was first modified with PEI.[48,49] It can be seen from the TEM image (Figure 3A) that the modified PEI has no side effect on the

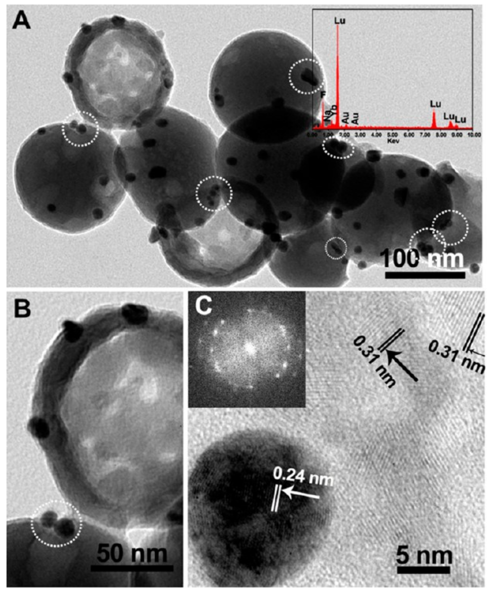

Figure 3. (A, B) TEM images and (C) HRTEM image of $Na_5Lu_9F_{32}$:Yb/Er@Au HMSs. Inset in panel A is the corresponding EDS pattern.

uniformity of the hollow spheres. Then Au NCs are successfully attached to the surface of $Na_5Lu_9F_{32}$:Yb/Er without free Au NCs left nearby, which reveals the good attachment of Au NCs to $Na_5Lu_9F_{32}$:Yb/Er. The magnified TEM image (Figure 3B) reveals that the particle size of the coated Au NCs is about 10 nm. We can also see that most of the Au NCs are single or coupled with each other with different distances which are mostly 0−10 nm. The HRTEM image in Figure 3C shows the apparent lattice fringes with an adjacent distance of 0.31 nm, corresponding to *d*-spacing of the (111) plane for cubic $Na_5Lu_9F_{32}$ (JCPDS No. 27-0725), and the distance of 0.24 nm matches with the interplanner distance of the (111) plane for cubic phased Au (JCPDS No. 04-0784).

A nitrogen adsorption/desorption experiment was employed to study the porous structure of $Na_5Lu_9F_{32}$:Yb/Er (Figure 4A) and $Na_5Lu_9F_{32}$:Yb/Er@Au (Figure 4B) hollow spheres. It can be seen that the two samples exhibit IV-typed isotherms with H1-hysteresis loops, which represents the characteristics of typical mesoporous materials.[50] The BET surface area and total pore volume of $Na_5Lu_9F_{32}$:Yb/Er were calculated to be 28.4 m^2/g and 0.064 cm^3/g, while the $Na_5Lu_9F_{32}$:Yb/Er@Au were calculated to be 24.4 m^2/g and 0.048 cm^3/g. The pore size distribution curves reveal that the pores of the two samples are irregular, and the respective average pore size is calculated to be 9.0 and 7.9 nm.[51] The mesoporous structure with high specific surface area is suitable as a drug carrier. As discussed above, the

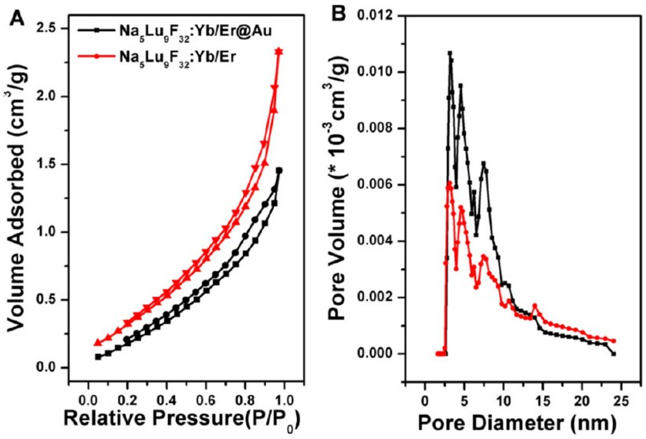

Figure 4. (A) Nitrogen adsorption/desorption isotherms and (B) corresponding pore size distribution curves of $Na_5Lu_9F_{32}$:Yb/Er and $Na_5Lu_9F_{32}$:Yb/Er@Au HMSs.

formation of $Na_5Lu_9F_{32}$:Yb/Er with Au NCs attached and the cell up-take process can be illustrated in Scheme 1.

Scheme 1. Schematic Illustration for the Formation and Application of $Na_5Lu_9F_{32}$:Yb/Er@Au HMSs

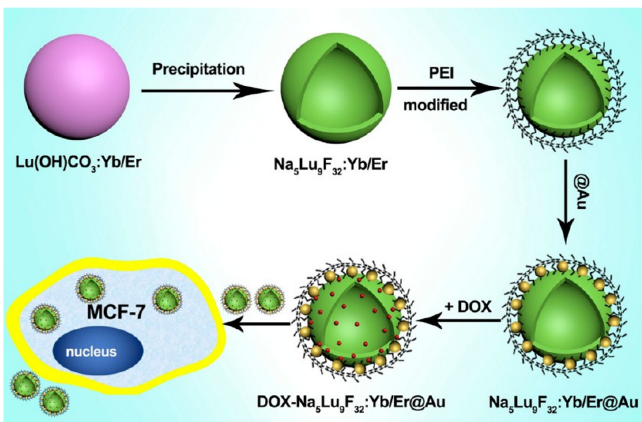

Photoluminescence Properties. Figure 5A,C, and E shows the UC emission spectra of $Na_5Lu_9F_{32}$:Ln under 980 nm LD irradiation. The spectrum of $Na_5Lu_9F_{32}$:15%Yb/1%Er (Figure 5A) contains four chief emission peaks at around 407, 522, 539, and 653 nm, corresponding to $^2H_{9/2} \rightarrow {}^4I_{15/2}$, $^2H_{11/2} \rightarrow {}^4I_{15/2}$, $^4S_{3/2} \rightarrow {}^4I_{15/2}$, and $^4F_{9/2} \rightarrow {}^4I_{15/2}$ transitions of Er^{3+}, respectively.[52,53] There are three main emission bands centered at 485, 540, and 644 nm in the UC emission spectrum of $Na_5Lu_9F_{32}$:15%Yb/1%Ho (Figure 5C), which can be attributed to $^5F_1 \rightarrow {}^5I_8$, $^5F_4/{}^5S_2 \rightarrow {}^5I_8$, and $^5F_5 \rightarrow {}^5I_8$ transitions of Ho^{3+}, respectively.[54,55] In Figure 5E, four peaks including 449, 475, 649, and 700 nm are represented in the emission spectrum of $Na_5Lu_9F_{32}$:15%Yb/1%Tm, and all the peaks can be associated with $^1D_2 \rightarrow {}^3F_4$, $^1G_4 \rightarrow {}^3H_6$, $^1G_4 \rightarrow {}^3F_4$, and $^3F_3 \rightarrow {}^3H_6$ transitions of Tm^{3+}, respectively.[56,57] The inset of Figure 5A−C represents the three samples that emit yellow, green, and purple light under 980 nm LD irradiation with high pump power of 1092 mW, respectively. Figure 5B, 5D, and 5F shows the respective ratios of blue, green, and red emissions between the integral intensity and dependent power. The ratios of blue emissions are 2.87 and 2.85, which indicates that the blue emissions are a three-photon energy-transfer process. The ratios of green emissions are 1.69 and 1.84, and the ratios of red emissions are 1.86, 1.92, and 1.82, which indicate that the green and red emissions are a two-photon energy transfer process. The energy-transfer mechanism of $Na_5Lu_9F_{32}$:Ln (Yb/Er, Yb/Ho, and Yb/Tm) using the energy level diagram is depicted in Figure 5F.

When Au NCs were modified on the surface of $Na_5Lu_9F_{32}$:Yb/Er, the spectra of $Na_5Lu_9F_{32}$:Yb/Er@Au with different pump powers are shown in Figure 6A. Note that these pump powers are much lower than that used in Figure 5 (1092 mW). Here, there are two reasons for the use of lower pump powers. First, it is well-known that up-conversion materials take advantage of energy transfer, and their high brightness originates from a combination of high excitation intensity, increased activator concentration, and accelerated sensitizer−activator energy transfer rate. Only the advanced up-conversion phosphors with proper host and dopant could emit strong luminescence under lower pump powers.[58,59] The suitable hosts such as lanthanide fluoride have been suggested to optimize brightness by increasing photon absorption and minimizing luminescence quenching. Second, as the potential luminescent material, the lower pumping power provides a wider choice for the users with different conditions because the overexposure under the 980 nm irradiation with longer time or higher powers could cause overheating issues which may bring damage to the cells and tissues. In the thermal detection and biological assay, we also used the lower irradiation power to regulate the thermal effect to a controllable extent.

In order to evaluate the effect of the Au NCs under different conditions, three compared groups of $Na_5Lu_9F_{32}$:Yb/Er and $Na_5Lu_9F_{32}$:Yb/Er@Au with different Au NC solution (1, 0.8, and 0.5 mL) added in to the $Na_5Lu_9F_{32}$:Yb/Er solution were prepared. The corresponding spectra and the corresponding enhancement factors were shown in Figure S4A-B, C-D, and E-F (Supporting Information), respectively. The typical spectra are shown in Figure 6A, and there are obvious luminescence enhancements in $Na_5Lu_9F_{32}$:Yb/Er@Au compared to that of $Na_5Lu_9F_{32}$:Yb/Er with every different pumping power. As shown in Figure S4B (Supporting Information), there is a higher enhancement factor in the blue region (407 nm) than in the green or red regions (522, 539, and 653 nm) when 1 mL of Au NC solution was added. However, as shown in Figure S4D and S4F (Supporting Information), the enhancement factors with the added solutions of 0.8 and 0.5 mL have no great distinctions. These factor variations between the samples with different Au NCs added are due to the SPR and LFE effects which will be discussed in the following. Figure 6B shows the enhancement factor of the four peaks irradiated under different pumping power. The standard deviations of the enhancement factors are high because the luminescent detection under lower pump powers is sensitive and the enhancement factor is diverse with a different amount of Au NC solution. However, we can still conclude that the luminescent intensities are enhanced in all emission regions under different low pump powers. The lifetimes of Er^{3+} in $Na_5Lu_9F_{32}$:Yb/Er and $Na_5Lu_9F_{32}$:Yb/Er@Au at 522 nm under 980 nm irradiation have also been detected (Figure 6C and 6D). Both of the decay curves can be well fitted into a single exponential function as $I = I_0 + A\exp(-t/\tau)$ (where τ is the 1/e lifetime of the Er^{3+} ion). The lifetime of Er^{3+} ions decreased from 1.75 to 0.61 ms after Au NCs were modified. There are two major effects when Au NCs approach to a phosphor: (1) LFE effect in the excitation increases the emission efficiency due to the increased disorder and energy

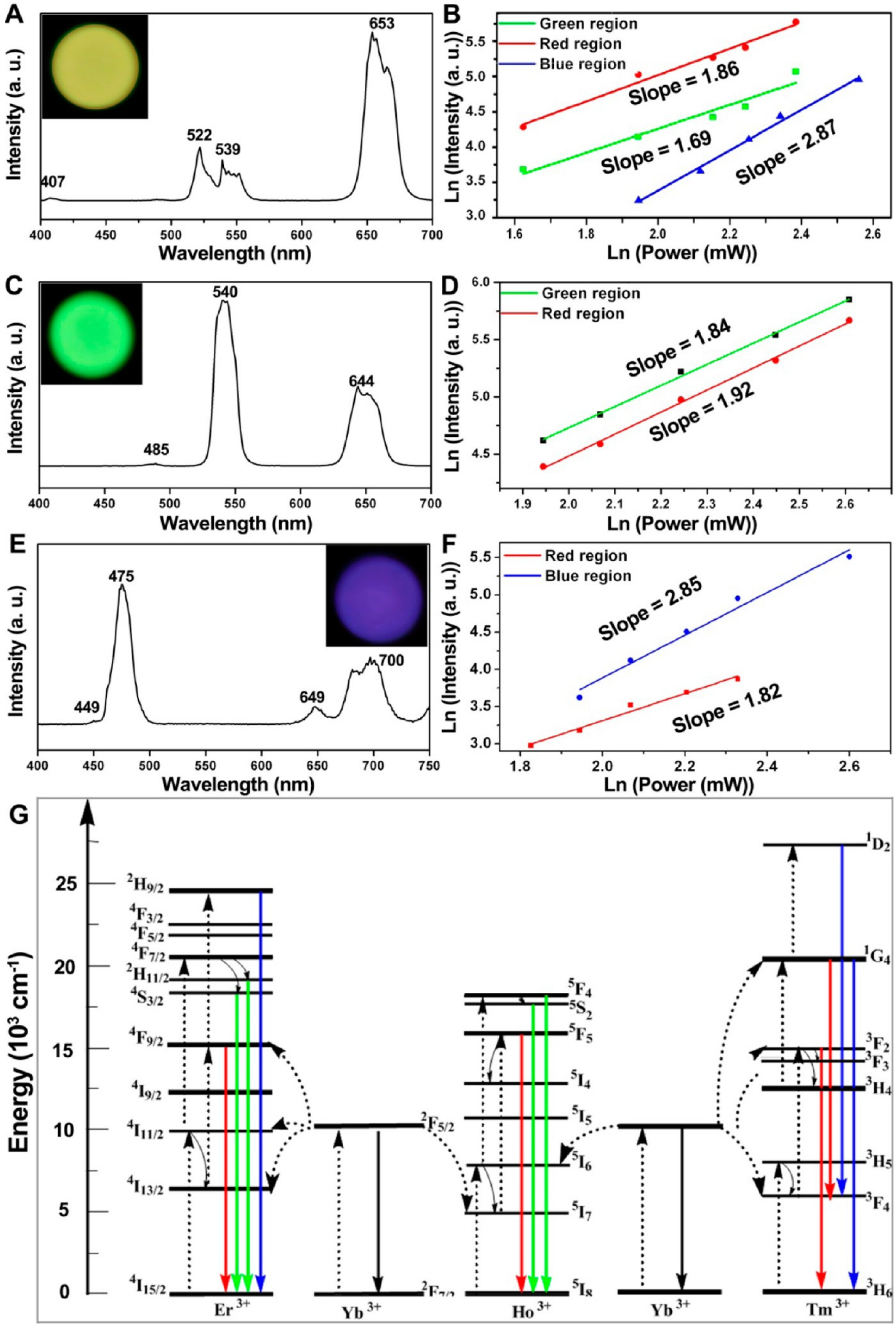

Figure 5. UC emission spectra and the emission intensities as a function of dependent pump power for (A, B) $Na_5Lu_9F_{32}$:Yb/Er, (C, D) $Na_5Lu_9F_{32}$:Yb/Ho, and (E, F) $Na_5Lu_9F_{32}$:Yb/Tm under 980 nm LD irradiation and (G) proposed energy transfer mechanism of Yb:Er/Ho/Tm.

deduced from Au NCs to the matrix.[60] (2) SPR absorption in the emission reduces fluorescence of the phosphor by energy transfer from the phosphor to Au NCs.[61] The two effects can change both the fluorescence lifetime and the intensity. Consequently, the pump power density of 980 nm excitation can be increased due to the LFE effect of Au NCs, resulting in increasing Yb^{3+} ions on the excited level which enhance the photons on the whole UC emission regions. Meanwhile, the lower enhancement in green and red regions and decreased lifetime are due to the SPR effect which effectively increases

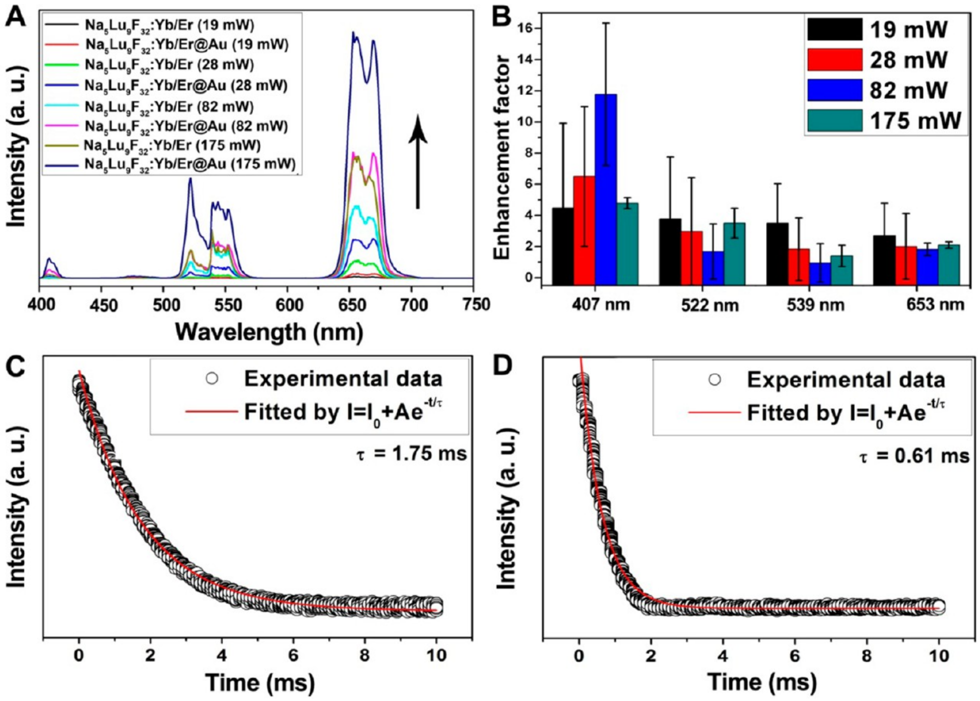

Figure 6. (A) UC emission spectra and (B) the corresponding enhancement factors of the emission intensity for $Na_5Lu_9F_{32}$:Yb/Er and $Na_5Lu_9F_{32}$:Yb/Er@Au HMSs with pump powers of 19, 28, 82, and 175 mW; the decay curves at the wavelength of 522 nm for (C) $Na_5Lu_9F_{32}$:Yb/Er and (D) $Na_5Lu_9F_{32}$:Yb/Er@Au under 980 nm irradiation.

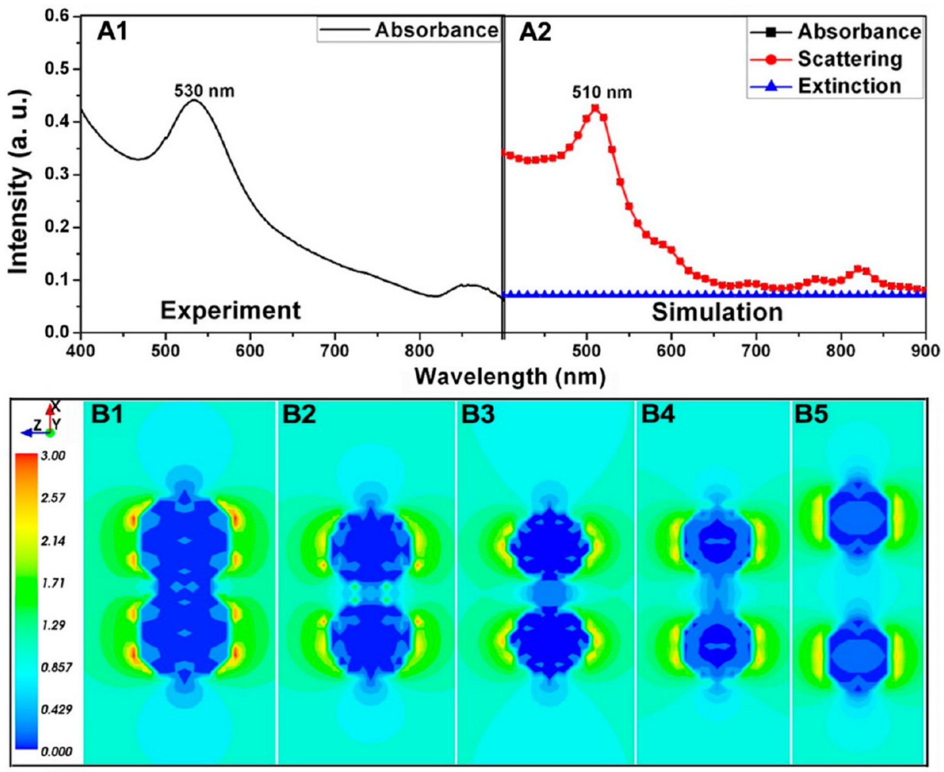

Figure 7. Absorption spectra of single Au nanocrystals with the (A1) experiment and (A2) simulation conditions with DDA simulation; the electric field strength ($|E|/|E_0|$) of two Au NCs at the wavelength of 980 nm with the distance of (B1) 0 nm, (B2) 1 nm, (B3) 3 nm, (B4) 5 nm, and (B5) 10 nm between the two spheres.

both the nonradiative (thermal effect) and radiative decay rates (shortened lifetimes).

To confirm the two effects of Au NCs on the UC process in theory, we used DDA calculation to investigate and predict the SPR peak and the strength of the LFE. The absorbance spectrum with the experiment is shown in Figure 7A1, and the simulation result of the Au NCs with the diameter of 10 nm is given in Figure 7A2. There is a wide peak around 530 nm in the absorbance of Au NCs (Figure 7A1). It is found that the absorbance in the simulation condition (Figure 7A2) is similar to the experimental spectrum. For the experiment, the region of the absorption peak is slightly wider than that of the simulated value, which is due to the single direction in the simulation condition. Besides, the scattering spectrum of Au NCs is negligible compared with the absorbance when referring to the SPR effect, and the scattering or absorbance which plays a main role in the extinction of Au NCs is decided by the diameter of the Au NCs. Figure S5 (Supporting Information) gives the scattering and absorbance spectra with different diameters, and it reveals that the main effect of Au NCs is the absorbance when the diameter is small.

When referring to the interactions of Au–Au NCs, two Au–Au interactions are typically used to simulate. This is because in TEM images (Figure 3A and 3B) there are two typical types of Au NCs: single and double. The electric field strength ($|E|/|E_0|$) of a single Au NC is shown in Figure S5B (Supporting Information). The strength around the sphere is uniform with the same value if the NIR light is irradiated in all views, and the irradiation is from the single direction under the simulation conditions. Figure 7B presents the electric field strength ($|E|/|E_0|$) at λ = 980 nm with the different distances between the two spheres when the medium is air with a refractive index of 1.33. We have calculated the strength with different distances of 0–10 nm. As shown in Figure 7B, when the distance between the two Au NCs is increased, the strength decreases. This local strength is beneficial to the UC luminescence as it is in the irradiation wavelength of 980 nm.[62] The enhancement factor in Figure 6B can represent the total effect of Au NCs of which the strength has the positive correlation and the SPR effect has the negative correlation. That means that even if the strength decreases the enhancement factor may decrease, but the luminescence intensity can also increase. The simulation can be proved by the experimental data (Figure S5, Supporting Information). Due to the interaction of positively charged PEI and negatively charged Au NCs, the amount of Au particles on the surface of the $Na_5Lu_9F_{32}$:Yb/Er HMSs could be regulated by the amount of Au solution. TEM images of $Na_5Lu_9F_{32}$:Yb/Er@Au with different Au NC solution added were shown in Figure S6 (Supporting Information), and when the amount of Au NC solution is increased, the distances between two Au particles are decreased. The UC spectra of $Na_5Lu_9F_{32}$:Yb/Er@Au with different Au NC solution added were detected and shown in Figure S7 (Supporting Information). The enhancement of luminescent intensity becomes higher with the increased amount of solution. When the added solution is increased to 1 mL, some enhancement factors of the red and green regions decrease the optimized value due to the increased SPR effect of Au NCs.[61,63] This is the main reason why only a small amount of Au NC solution was added (not more than 1 mL).

Figure 8A presents the temperatures of $Na_5Lu_9F_{32}$:Yb/Er and $Na_5Lu_9F_{32}$:Yb/Er@Au HMSs with the increased time under 980 nm irradiation. $Na_5Lu_9F_{32}$:Yb/Er@Au has a rapid increased temperature, and the final temperature is higher than $Na_5Lu_9F_{32}$:Yb/Er, indicating more nonradiative transition occurs for $Na_5Lu_9F_{32}$:Yb/Er@Au due to the SPR effect. The corresponding infrared thermal images of $Na_5Lu_9F_{32}$ (Figure S8, Supporting Information) and $Na_5Lu_9F_{32}$:Yb/Er@Au (Figure S9, Supporting Information) with prolonged time were taken under 980 nm laser irradiation. These images directly show the thermal effect of Au NCs. Figure 8B gives the

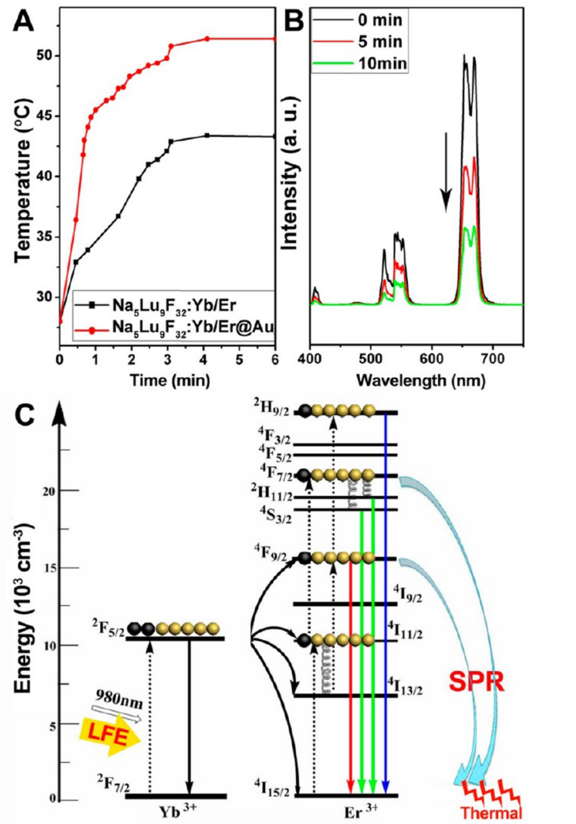

Figure 8. (A) Temperatures, (B) UC emission spectra with the increase of time for $Na_5Lu_9F_{32}$:Yb/Er and $Na_5Lu_9F_{32}$:Yb/Er@Au under 980 nm LD irradiation, and (C) energy-transfer mechanism of $Na_5Lu_9F_{32}$:Yb/Er@Au using the energy level diagram.

UC luminescent spectra of $Na_5Lu_9F_{32}$:Yb/Er@Au with increased time, and it shows that the emission decreases obviously with the increase of irradiation time. These decreased emissions can be explained from the temperature quenching caused by the thermal effect of Au NCs, which is caused by the nonradiative transitions.[64−66]

The energy-transfer mechanism of $Na_5Lu_9F_{32}$:Yb/Er@Au is depicted in Figure 8C using the energy level diagram. On one side, the enhanced UC emissions in all visible regions are achieved due to the LFE effect which increases the activated photons in the higher energy levels. On the other side, the decreased enhancement in the green and red regions, the shortened lifetime, and the increased nonradiative transitions are attributed to the SPR effect. It is well-known that the thermal effect caused by the nonradiative transitions could regulate the release property; hence, the as-prepared $Na_5Lu_9F_{32}$:Yb/Er@Au HMSs should be good material as a drug carrier, while the enhanced UC luminescence is beneficial to the bioimaging.

Cell Viability, Drug Release, and MTT Cytotoxicity Assay. In this report, the UC luminescent spectra of the hollow mesoporous samples were all detected with the solid phosphors instead of the solution. In order to evaluate the emissions under NIR irradiation in the solution, we have taken the dynamic light scattering (DLS) analysis of the $Na_5Lu_9F_{32}$:Yb/Er@Au HMSs in the PBS solution (pH = 7.2) which is shown in Figure S10 (Supporting Information). The average diameter value is 204 nm, which is a little larger than that obtained by TEM. Note that the DLS technique measures the hydrodynamic size of the $Na_5Lu_9F_{32}$:Yb/Er@Au HMSs surrounded by the PEI layer.

The photographs of the $Na_5Lu_9F_{32}$:Yb/Er@Au solutions dissolved by water with different concentrations of $Na_5Lu_9F_{32}$:Yb/Er@Au (10, 5, and 1 mg/mL) were detected (Figure S11A1−A3, Supporting Information). The UC luminescent emissions of $Na_5Lu_9F_{32}$:Yb/Er solution (Figure S10B1−B3, Supporting Information) and $Na_5Lu_9F_{32}$:Yb/Er@Au solution (Figure S10C1−C3, Supporting Information) under the 980 nm irradiation were also detected. When the solutions keep stable under the same concentrations (10 and 5 mg/mL), the scattering effect in $Na_5Lu_9F_{32}$:Yb/Er and $Na_5Lu_9F_{32}$:Yb/Er@Au almost has the same result. In this condition, the NIR excitation could penetrate the medium, while the UC emissions in the visible region with shorter wavelengths are scattered due to the Rayleigh scattering effect. Thus, the visible zones are limited with higher concentrations. Meanwhile, there is almost the same scattering rate between $Na_5Lu_9F_{32}$:Yb/Er and $Na_5Lu_9F_{32}$:Yb/Er@Au solutions with high concentrations (B1 to C1 and B2 to C2). When the concentrations decrease to 1 mg/mL which is always the highest concentration used when assaying the cell viability and cytotoxicity in vitro or intravenous injection in vivo, the solution is almost transparent, and there is an emission band (B3 and C3). Thus, the scattering effect could be neglected in this report.

For potential biological applications, it is essential to evaluate the biocompatibility of $Na_5Lu_9F_{32}$:Yb/Er@Au HMSs. A standard MTT cell assay was carried out with L929 cell lines in order to detect the viability. Figure 9A demonstrates the cell viability with different concentrations of the particles varying from 7.8125 to 250 μg/mL incubated for 24 h. It is obvious that the cell viability of the as-prepared material in all dosages is up to 98.51−104.71%. Even incubated at high concentration of 250 μg/mL, the viability of the L929 cell is 102.58%. These data demonstrated that the as-prepared $Na_5Lu_9F_{32}$:Yb/Er@Au HMSs are nontoxic to live cells. Meanwhile, it is important to detect the biocompatibility of the sample with blood cells to guarantee the successful intravenous administration as the anticancer chemotherapy (Figure 9B). During the hemolysis assay process, the obtained red solution dissolved with H_2O is caused by the hemoglobin released into the solution, while for the controlled tubes with the PBS and the sample with different concentrations added there is no obvious visual red occurring, indicating there is no or negligible hemolysis. The highest hemolytic efficiency with different material concentrations from 7.81 to 250 μg/mL is 0.17%, which indicates $Na_5Lu_9F_{32}$:Yb/Er@Au is almost not hemolytic. Thus, it is inferred that the blood compatibility of the as-synthesized product is excellent.

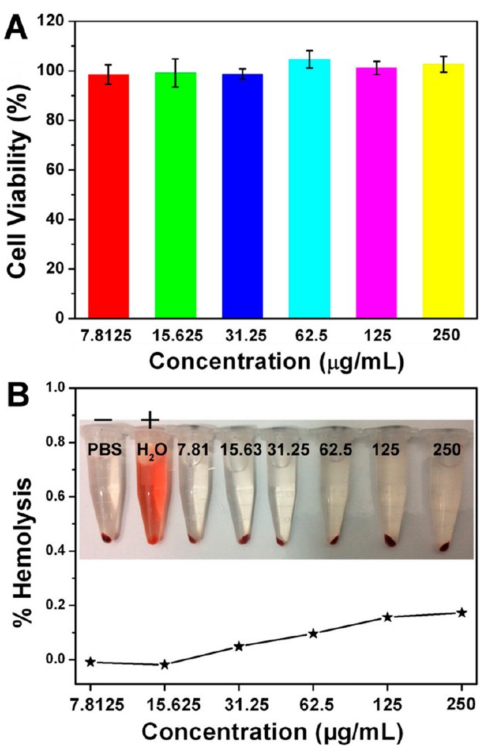

Figure 9. (A) Cell viability of $Na_5Lu_9F_{32}$:Yb/Er@Au HMSs incubated with L929 cells using standard MTT assay and (B) the hemolysis percentage of $Na_5Lu_9F_{32}$:Yb/Er@Au HMSs to human red blood cells.

DOX as a regular anticancer drug was used as a model drug to evaluate the loading and release behavior,[67,68] and pH values of 4 and 7 were selected to demonstrate the release efficiency, which usually represents the environment of the cancer cell and normal cell, respectively. To study the interaction between the as-prepared $Na_5Lu_9F_{32}$:Yb/Er@Au HMSs and the loaded DOX, we have detected the FT-IR spectra of the precursor, PEI-modified $Na_5Lu_9F_{32}$:Yb/Er@Au, and DOX-loaded $Na_5Lu_9F_{32}$:Yb/Er@Au HMSs, which are shown in Figure S12 (Supporting Information). A similar band in all the three samples at 3100−3700 and 1082 cm^{-1} can be assigned to the −OH stretching and bending vibrations of water and hydroxyl groups. For the precursor, the characteristic absorption bands of O−C−O (1523 and 1401 cm^{-1}), π-CO_3^{2-} (843 cm^{-1}), and δ-CO_3^{2-} (753 and 688 cm^{-1}) can be observed. After PEI modification, the unique absorption peaks at 1640, 1443, and 1392 cm^{-1} from the internal vibration of $-NH_2$ and −CN reveal the presence of PEI.[49] When the Au NCs were modified on $Na_5Lu_9F_{32}$:Yb/Er and the DOX was loaded, the unique band at 1617 cm^{-1} is ascribed to the stretching vibrations of C═O in DOX, providing the additional evidence for the loading of DOX molecules on $Na_5Lu_9F_{32}$:Yb/Er@Au. It is obvious that the $-NH_2$ and −CN still existed in the $Na_5Lu_9F_{32}$:Yb/Er@Au HMSs, which reveals that the PEI still plays a key role in the loading process. From the TEM images in Figure 3A,B, we can also see that the Au NCs did not coat wholly on the surface of $Na_5Lu_9F_{32}$:Yb/Er because only a small amount of Au NC solution was added. After continuous stirring for 24 h, DOX has been mostly convergent to $Na_5Lu_9F_{32}$:Yb/Er@Au with loading efficiency of 72.8% (with an amount of 0.18 mg). The high loading amount of DOX is due to the hollow mesoporous structure of the $Na_5Lu_9F_{32}$:Yb/Er@Au. The released efficiencies of $Na_5Lu_9F_{32}$:Yb/Er@Au HMSs with and without NIR irradiation were tested under different pH environments as shown in Figure 10A. When there is no irradiation, the final released ratio is 81.9% with the pH value of 4, while the released ratio decreases to 48.4% with the pH value of 7. In the initial 1 h, the released efficiencies are 32.9% and 18.6%, respectively. When the irradiation is introduced, the final released ratio is 95.7% with the pH value of 4, and the ratio is 59.0% with the pH value of 7. This result reveals that the thermal effect of Au NCs may promote the release amount. In the two release processes, both of them have two steps in the released process: the initially rapid release which is caused by the diffusion and the slow release which is due to the channels and pores of $Na_5Lu_9F_{32}$:Yb/Er@Au HMSs.

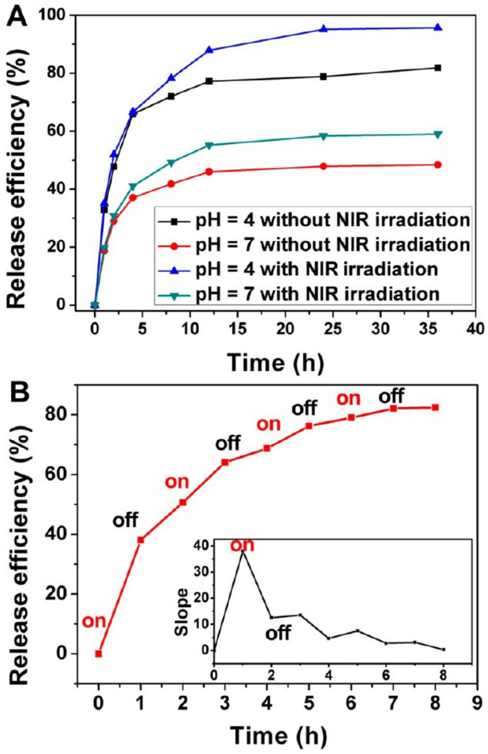

Figure 10. (A) DOX release efficiencies at different pH values with and without the NIR irradiation and (B) the release efficiency with irradiation on or off every 1 h for $Na_5Lu_9F_{32}$:Yb/Er@Au HMSs.

In order to further utilize the thermal effect of the Au NCs under a NIR laser to realize an "on/off" pattern and control the release process of the DDSs, the release efficiency of $Na_5Lu_9F_{32}$:Yb/Er@Au HMSs with the NIR laser on and off during 8 h was monitored by exposing the solution to alternating hours. The $Na_5Lu_9F_{32}$:Yb/Er@Au solution under investigation was irradiated by the 980 nm NIR laser in a 1 cm length quartz cuvette. During the released period, the sample (with or without NIR laser) was shaken for 1 min at 1 h intervals. Figure 10B reveals that the release efficiency with the NIR laser on during the same time interval (1 h) was up to 3 times that with the irradiation off. It is obvious that the released rate is fast with the NIR light on. That is, the absorbance of the gold particles makes the temperature increase due to the SPR effect which reduces local emission intensities and the lifetime but is beneficial to the drug release with a higher rate. Through controlling the sample exposed to a laser or not, the dose of the released drug could be regulated according to the specific condition. The initial rapid release of DOX molecules is essential to cure cancer, and the slow release of the rest of the drug molecules can be continued for curbing the few surviving cells. There is no doubt that the $Na_5Lu_9F_{32}$:Yb/Er@Au HMSs show a good drug delivery and release property. More importantly, the NIR light could potentially be used as the "on/off" regulator to control the release rate and efficiency.

As shown in Figure 11, which shows incubation with $Na_5Lu_9F_{32}$:Yb/Er@Au HMSs, more than 92.4% HeLa cells are viable under a wide concentration range (15.63–500 μg/mL). In comparison, even with the low concentration, both $Na_5Lu_9F_{32}$:Yb/Er@Au-DOX and pure DOX have high cytotoxicity to HeLa tumor cells, suggesting the high potential of the $Na_5Lu_9F_{32}$:Yb/Er@Au as the anticancer drug carrier. Meanwhile, the IC_{50} value of $Na_5Lu_9F_{32}$:Yb/Er@Au-DOX

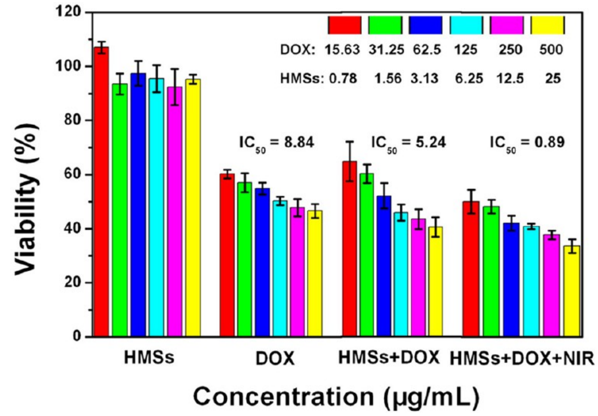

Figure 11. Viability of HeLa cells incubated with $Na_5Lu_9F_{32}$:Yb/Er@Au HMSs, free DOX, $Na_5Lu_9F_{32}$:Yb/Er@Au + DOX, and $Na_5Lu_9F_{32}$:Yb/Er@Au + DOX with NIR irradiated using the standard MTT assay.

(5.24) is lower than that of free DOX (8.84) to HeLa cells, indicating the higher inhibition of the as-prepared drug carrier. More importantly, when incubated with $Na_5Lu_9F_{32}$:Yb/Er@Au + DOX under 980 nm laser irradiation, HeLa cells were inhibited higher with the viability of 33.6%–50.1%. The IC_{50} was only 0.89, which means the cytotoxicity of HMSs + DOX with NIR irradiated is highly enhanced. In conclusion, the NIR light triggers the drug release, generates a thermal effect, and finally results in a higher antitumor effect.

Figure 12 gives the inverted florescence microscope images of HeLa cells incubated with $Na_5Lu_9F_{32}$:Yb/Er@Au for 1 and 3

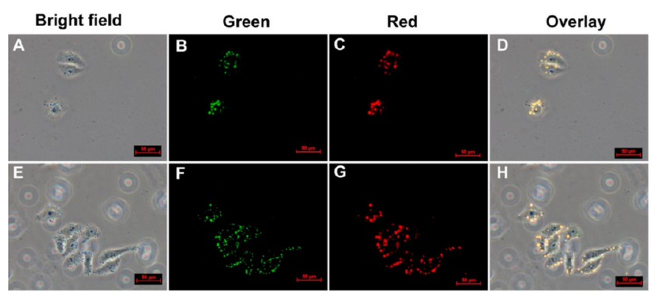

Figure 12. Inverted fluorescence microscope images of HeLa cells incubated with $Na_5Lu_9F_{32}$:Yb/Er@Au for (A–D) 1 h and (E–H) 3 h.

h at 37 °C. The confocal microscope is equipped with a 980 nm NIR laser. The up-conversion luminescent signals at green and red regions were detected, respectively. Bright-field and overlays of confocal luminescence images further demonstrate that the HMSs are evident in the intracellular region, and no luminescent signal outside of the cells is measured, suggesting that the HMSs have been internalized into the cells rather than merely staining on the membrane surface.[69,70] Also, it can be seen that with the prolonging of incubation time the luminescence intensity increased, indicating that more and more HMSs were taken up by the cells. These observations demonstrate that the as-prepared $Na_5Lu_9F_{32}$:Yb/Er@Au HMSs are promising candidates for high-contrast in vitro bioimaging with negligible background.

The CLSM photographs of HeLa cancer cells incubated with as-prepared $Na_5Lu_9F_{32}$:Yb/Er@Au + DOX for 30 min, 3 h, and 6 h at 37 °C were further taken in order to verify the cell uptake process. As shown in Figure 13, each series can be classified

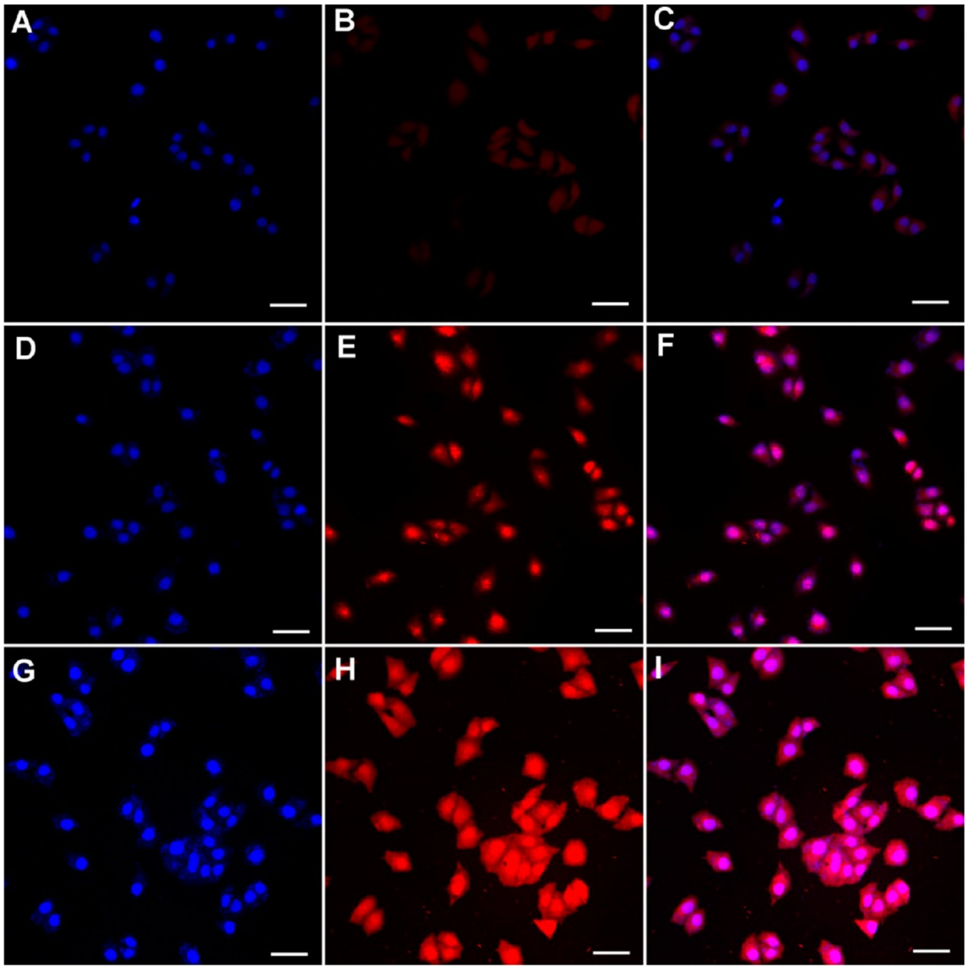

Figure 13. Confocal laser scanning microscopy (CLSM) images of HeLa cancer cells incubated with $Na_5Lu_9F_{32}$:Yb/Er@Au + DOX for (A−C) 30 min, (D−F) 3 h, and (G−I) 6 h at 37 °C. Scale bars for all images are 50 μm.

into the nuclei of cells (dyed blue by DAPI), $Na_5Lu_9F_{32}$:Yb/Er@Au + DOX, and an overlay of the two channels, respectively. The excitation wavelengths of DAPI and DOX are 405 and 543 nm, respectively, and the red emission is derived from DOX molecules. In the first 30 min, there is little red emission, which indicates only a few drugs were taken up by the cells. When the incubation time was increased to 3 h, stronger red emissions were detected. The red fluorescence of DOX was observed in both the cytoplasm and the cell nucleus. Finally, almost all of the composites have crossed the membrane and are localized in the cytoplasm with the increased incubation time of 6 h. Through the time course CLSM results, it can be concluded that as-prepared samples can be effectively taken up by cancer cells.

CONCLUSIONS

In this report, uniform $Na_5Lu_9F_{32}$:Yb/Er hollow mesoporous spheres have been successfully prepared by a facile coprecipitation process under mild reaction conditions. After Au NC conjugation, the UC luminescence intensity of $Na_5Lu_9F_{32}$:Yb/Er@Au HMSs was improved under low pump power due to the local field enhancement, and there is a SPR effect which decreases the local emission but generates a thermal effect. The advanced properties have been proved by DDA simulation. Meanwhile, the good biocompatibility and sustained DOX release properties indicate it is a promising candidate in cancer therapy. In particular, under NIR laser irradiation, a rapid DOX release was achieved due to the thermal effect of gold NCs. Furthermore, UC luminescence images of $Na_5Lu_9F_{32}$:Yb/Er@Au HMSs uptaken by cells shows bright green and red emissions compared with $Na_5Lu_9F_{32}$:Yb/Er HMSs under 980 nm laser excitation. This novel multifunctional (mesoporous, enhanced UC luminescent, and thermal) drug delivery system should have potential as a suitable candidate for targeted cancer therapy carriers and bioimaging.

ASSOCIATED CONTENT

Supporting Information

Additional experimental details. The UV−vis absorption spectrum and calibration curve of DOX solution. TEM images of the precursor of $Na_5Lu_9F_{32}$:Yb/Er. TEM images of $Na_5Lu_9F_{32}$:Yb/Er prepared at different reaction times. The spectra of the $Na_5Lu_9F_{32}$:Yb/Er and $Na_5Lu_9F_{32}$:Yb/Er@Au and enhancement factor with different Au NC solution. The intensity of single Au nanocrystals with different diameters calculated by DDA simulation; the electric field strength ($|E|/|E_0|$) of a single Au NC irradiated at the wavelength of 980 nm. TEM images of $Na_5Lu_9F_{32}$:Yb/Er@Au with different Au NC solution added. UC luminescence spectra of $Na_5Lu_9F_{32}$:Yb/Er@Au prepared with different amounts of Au NC solution. Infrared thermal image of the $Na_5Lu_9F_{32}$:Yb/Er sample under

980 nm laser irradiation with different times. Infrared thermal image of the $Na_5Lu_9F_{32}$:Yb/Er@Au sample under 980 nm laser irradiation with different times. Dynamic light scattering (DLS) analysis of the $Na_5Lu_9F_{32}$:Yb/Er@Au HMSs. Photographs of solutions with various concentrations of $Na_5Lu_9F_{32}$:Yb/Er@Au, UC luminescent emissions of $Na_5Lu_9F_{32}$:Yb/Er solution, and $Na_5Lu_9F_{32}$:Yb/Er@Au solution under the 980 nm irradiation. FT-IR spectra of the precursor, PEI-modified $Na_5Lu_9F_{32}$:Yb/Er, and $Na_5Lu_9F_{32}$:Yb/Er@Au + DOX. This material is available free of charge via the Internet at http://pubs.acs.org.

■ AUTHOR INFORMATION

Corresponding Authors

*E-mail: yangpiaoping@hrbeu.edu.cn

*E-mail: jlin@ciac.ac.cn.

Notes

The authors declare no competing financial interest.

■ ACKNOWLEDGMENTS

Financial support from the National Natural Science Foundation of China (NSFC 21271053, 51472058, 21401032) is greatly acknowledged.

■ REFERENCES

(1) Peer, D.; Karp, J. M.; Hong, S.; FaroKhzad, O. C.; Margalit, R.; Langer, R. Nanocarriers as an Emerging Platform for Cancer Therapy. *Nat. Nanotechnol.* **2007**, *2*, 751−760.

(2) Yang, P.; Gai, S.; Lin, J. Functionalized Mesoporous Silica Materials for Controlled Drug Delivery. *Chem. Soc. Rev.* **2012**, *41*, 3679−3698.

(3) He, Q.; Shi, J. Mesoporous Silica Nanoparticle Based Nano Drug Delivery Systems: Synthesis, Controlled Drug Release and Delivery, Pharmacokinetics and Biocompatibility. *J. Mater. Chem.* **2011**, *21*, 5845−5855.

(4) Tian, L.; Yang, X.; Lu, P.; Williams, I. D.; Wang, C.; Ou, S.; Liang, C.; Wu, M. Hollow Single-crystal Spinel Nanocubes: The Case of Zinc Cobalt Oxide Grown by a Unique Kirkendall Effect. *Inorg. Chem.* **2008**, *47*, 5522−5524.

(5) Lou, X. W.; Archer, L. A.; Yang, Z. Hollow Micro-/ Nanostructures: Synthesis and Applications. *Adv. Mater.* **2008**, *20*, 3987−4019.

(6) Gai, S.; Li, C.; Yang, P.; Lin, J. Recent Progress in Rare Earth Micro/Nanocrystals: Soft Chemical Synthesis, Luminescent Properties, and Biomedical Applications. *Chem. Rev.* **2013**, *114*, 2343−2389.

(7) Nam, J.; Won, N.; Jin, H.; Chung, H.; Kim, S. pH-Induced Aggregation of Gold Nanoparticles for Photothermal Cancer Therapy. *J. Am. Chem. Soc.* **2009**, *131*, 13639−13645.

(8) Agasti, S. S.; Chompoosor, A.; You, C.-C.; Ghosh, P.; Kim, C. K.; Rotello, V. M. Photoregulated Release of Caged Anticancer Drugs from Gold Nanoparticles. *J. Am. Chem. Soc.* **2009**, *131*, 5728−5729.

(9) Zhang, F.; Braun, G. B.; Pallaoro, A.; Zhang, Y.; Shi, Y.; Cui, D.; Moskovits, M.; Zhao, D.; Stucky, G. D. Mesoporous Multifunctional Upconversion Luminescent and Magnetic "Nanorattle" Materials for Targeted Chemotherapy. *Nano Lett.* **2012**, *12*, 61−67.

(10) Kramer, K. W.; Biner, D.; Frei, G.; Gudel, H. U.; Hehlen, M. P.; Luthi, S. R. Hexagonal Sodium Yttrium Fluoride Based Green and Blue Emitting Upconversion Phosphors. *Chem. Mater.* **2004**, *16*, 1244−1251.

(11) Hischemoeller, A.; Nordmann, J.; Ptacek, P.; Mummenhoff, K.; Haase, M. In-vivo Imaging of the Uptake of Upconversion Nanoparticles by Plant Roots. *J. Biomed. Nanotechnol.* **2009**, *5*, 278−284.

(12) Altinoglu, E. i.; Russin, T. J.; Kaiser, J. M.; Barth, B. M.; Eklund, P. C.; Kester, M.; Adair, J. H. Near-infrared Emitting Fluorophore-doped Calcium Phosphate Nanoparticles for in vivo Imaging of Human Breast Cancer. *ACS Nano* **2008**, *2*, 2075−2084.

(13) Liu, F.; He, X.; Liu, L.; You, H.; Zhang, H.; Wang, Z. Conjugation of NaGdF4 Upconverting Nanoparticles on Silica Nanospheres as Contrast Agents for Multi-modality Imaging. *Biomaterials* **2013**, *34*, 5218−5225.

(14) Macedo, A. G.; Ferreira, R. A. S.; Ananias, D.; Reis, M. S.; Amaral, V. S.; Carlos, L. D.; Rocha, J. Effects of Phonon Confinement on Anomalous Thermalization, Energy Transfer, and Upconversion in Ln^{3+}-doped Gd_2O_3 Nanotubes. *Adv. Funct. Mater.* **2010**, *20*, 624−634.

(15) Liu, Y.; Tu, D.; Zhu, H.; Chen, X. Lanthanide-doped Luminescent Nanoprobes: Controlled Synthesis, Optical Spectroscopy, and Bioapplications. *Chem. Soc. Rev.* **2013**, *42*, 6924−6958.

(16) Cho, H.-J.; Yoon, H. Y.; Koo, H.; Ko, S.-H.; Shim, J.-S.; Lee, J.-H.; Kim, K.; Kwon, I. C.; Kim, D.-D. Self-assembled Nanoparticles based on Hyaluronic Acid-ceramide (HA-CE) and Pluronic (R) for Tumor-targeted Delivery of Docetaxel. *Biomaterials* **2011**, *32*, 7181−7190.

(17) Sivakumar, R.; van Veggel, F.; Raudsepp, M. Bright White Light through Up-conversion of a Single NIR Source from Sol-gel-derived Thin Film Made with Ln^{3+}-doped LaF_3 Nanoparticles. *J. Am. Chem. Soc.* **2005**, *127*, 12464−12465.

(18) Wang, F.; Banerjee, D.; Liu, Y.; Chen, X.; Liu, X. Upconversion Nanoparticles in Biological Labeling, Imaging, and Therapy. *Analyst* **2010**, *135*, 1839−1854.

(19) Liu, F.; Zhao, Q.; You, H.; Wang, Z. Synthesis of Stable Carboxy-terminated $NaYF_4:Yb^{3+}$, $Er^{3+}@SiO_2$ Nanoparticles with Ultrathin Shell for Biolabeling Applications. *Nanoscale* **2013**, *5*, 1047−1053.

(20) Chatteriee, D. K.; Rufalhah, A. J.; Zhang, Y. Upconversion Fluorescence Imaging of Cells and Small Animals using Lanthanide doped Nanocrystals. *Biomaterials* **2008**, *29*, 937−943.

(21) Wang, F.; Han, Y.; Lim, C. S.; Lu, Y.; Wang, J.; Xu, J.; Chen, H.; Zhang, C.; Hong, M.; Liu, X. Simultaneous Phase and Size Control of Upconversion Nanocrystals through Lanthanide doping. *Nature* **2010**, *463*, 1061−1065.

(22) He, X.; Yan, B. A novel Sc^{3+}-containing Fluoride Host Material for Down- and Up-Conversion Luminescence. *J. Mater. Chem. C* **2013**, *1*, 3910−3912.

(23) Zhou, J.; Liu, Z.; Li, F. Upconversion Nanophosphors for Small-animal Imaging. *Chem. Soc. Rev.* **2012**, *41*, 1323−1349.

(24) Heer, S.; Kompe, K.; Gudel, H. U.; Haase, M. Highly Efficient Multicolour Upconversion Emission in Transparent Colloids of Lanthanide-doped $NaYF_4$ Nanocrystals. *Adv. Mater.* **2004**, *16*, 2102−2105.

(25) Zheng, W.; Zhou, S.; Chen, Z.; Hu, P.; Liu, Y.; Tu, D.; Zhu, H.; Li, R.; Huang, M.; Chen, X. Sub-10nm Lanthanide-doped CaF_2 Nanoprobes for Time-resolved Luminescent Biodetection. *Angew. Chem., Int. Ed.* **2013**, *52*, 6671−6676.

(26) Zhuang, J.; Liang, L.; Sung, H. H. Y.; Yang, X.; Wu, M.; Williams, I. D.; Feng, S.; Su, Q. Controlled Hydrothermal Growth and Up-conversion Emission of $NaLnF_4$ (Ln = Y, Dy-Yb). *Inorg. Chem.* **2007**, *46*, 5404−5410.

(27) Zhang, Q.; Yan, B. Phase Control of Upconversion Nanocrystals and New Rare Earth Fluorides though a Diffusion-controlled Strategy in a Hydrothermal System. *Chem. Commun.* **2011**, *47*, 5867−5869.

(28) Wang, Z.-L.; Hao, J.; Chan, H. L. W.; Wong, W.-T.; Wong, K.-L. A Strategy for Simultaneously Realizing the Cubic-to-Hexagonal Phase Transition and Controlling the Small Size of $NaYF_4:Yb^{3+},Er^{3+}$ Nanocrystals for in vitro Cell Imaging. *Small* **2012**, *8*, 1863−1868.

(29) Yan, R. X.; Li, Y. D. Down/up Conversion in Ln^{3+}-doped YF_3 Nanocrystals. *Adv. Funct. Mater.* **2005**, *15*, 763−770.

(30) Liu, R.; Tu, D.; Liu, Y.; Zhu, H.; Li, R.; Zheng, W.; Ma, E.; Chen, X. Controlled Synthesis and Optical Spectroscopy of Lanthanide-doped $KLaF_4$ Nanocrystals. *Nanoscale* **2012**, *4*, 4485−4491.

(31) Liu, H.; Lu, W.; Wang, H.; Rao, L.; Yi, Z.; Zeng, S.; Hao, J. Simultaneous Synthesis and Amine-functionalization of Single-phase $BaYF_5$:Yb/Er Nanoprobe for Dual-modal in vivo Upconversion Fluorescence and Long-lasting X-ray Computed Tomography Imaging. *Nanoscale* **2013**, *5*, 6023−6029.

(32) Boyer, J. C.; Vetrone, F.; Cuccia, L. A.; Capobianco, J. A. Synthesis of Colloidal Upconverting $NaYF_4$ Nanocrystals doped with Er^{3+}, Yb^{3+}, and Tm^{3+}, Yb^{3+} via Thermal Decomposition of Lanthanide Trifluoroacetate Precursors. *J. Am. Chem. Soc.* **2006**, *128*, 7444−7445.

(33) Wang, F.; Deng, R.; Wang, J.; Wang, Q.; Han, Y.; Zhu, H.; Chen, X.; Liu, X. Tuning Upconversion through Energy Migration in Core-Shell Nanoparticles. *Nat. Mater.* **2011**, *10*, 968−973.

(34) Stouwdam, J. W.; van Veggel, F. Improvement in the Luminescence Properties and Processability of LaF_3/Ln and $LaPO_4$/Ln Nanoparticles by Surface Modification. *Langmuir* **2004**, *20*, 11763−11771.

(35) Jain, P. K.; Huang, X.; El-Sayed, I. H.; El-Sayed, M. A. Noble Metals on the Nanoscale: Optical and Photothermal Properties and Some Applications in Imaging, Sensing, Biology, and Medicine. *Acc. Chem. Res.* **2008**, *41*, 1578−1586.

(36) Zhang, Y.; Hao, J. Metal-ion doped Luminescent Thin Films for Optoelectronic Applications. *J. Mater. Chem. C* **2013**, *1*, 5607−5618.

(37) Zhang, S.; Ni, W.; Kou, X.; Yeung, M. H.; Sun, L.; Wang, J.; Yan, C. Formation of Gold and Silver Nanoparticle Arrays and Thin Shells on Mesostructured Silica Nanofibers. *Adv. Funct. Mater.* **2007**, *17*, 3258−3266.

(38) Chen, H.; Sun, Z.; Ni, W.; Woo, K. C.; Lin, H.-Q.; Sun, L.; Yan, C.; Wang, J. Plasmon Coupling in Clusters Composed of Two-Dimensionally Ordered Gold Nanocubes. *Small* **2009**, *5*, 2111−2119.

(39) Zhang, H.; Xu, D.; Huang, Y.; Duan, X. Highly Spectral Dependent Enhancement of Upconversion Emission with Sputtered Gold Island Films. *Chem. Commun.* **2011**, *47*, 979−981.

(40) Logsdail, A. J.; Johnston, R. L. Predicting the Optical Properties of Core-Shell and Janus Segregated Au-M Nanoparticles (M = Ag, Pd). *J. Phys. Chem. C* **2012**, *116*, 23616−23628.

(41) Mahmoud, M. A.; O'Neil, D.; El-Sayed, M. A. Hollow and Solid Metallic Nanoparticles in Sensing and in Nanocatalysis. *Chem. Mater.* **2014**, *26*, 44−58.

(42) Liu, Y.; Zhou, S.; Tu, D.; Chen, Z.; Huang, M.; Zhu, H.; Ma, E.; Chen, X. Amine-Functionalized Lanthanide-doped Zirconia Nanoparticles: Optical Spectroscopy, Time-resolved Fluorescence Resonance Energy Transfer Biodetection, and Targeted Imaging. *J. Am. Chem. Soc.* **2012**, *134*, 15083−15090.

(43) Neupane, B.; Zhao, L.; Wang, G. Up-conversion Luminescence of Gold Nanospheres when Excited at Nonsurface Plasmon Resonance Wavelength by a Continuous Wave Laser. *Nano Lett.* **2013**, *13*, 4087−4092.

(44) Wang, G.; Peng, Q.; Li, Y. Lanthanide-doped Nanocrystals: Synthesis, Optical-magnetic Properties, and Applications. *Acc. Chem. Res.* **2011**, *44*, 322−332.

(45) Cheng, L.; Yang, K.; Li, Y.; Chen, J.; Wang, C.; Shao, M.; Lee, S.-T.; Liu, Z. Facile Preparation of Multifunctional Upconversion Nanoprobes for Multimodal Imaging and Dual-Targeted Photothermal Therapy. *Angew. Chem., Int. Ed.* **2011**, *50*, 7385−7390.

(46) Zhang, F.; Shi, Y.; Sun, X.; Zhao, D.; Stucky, G. D. Formation of Hollow Upconversion Rare-earth Fluoride Nanospheres: Nanoscale Kirkendall Effect during Ion Exchange. *Chem. Mater.* **2009**, *21*, 5237−5243.

(47) Liang, X.; Wang, X.; Zhuang, Y.; Xu, B.; Kuang, S.; Li, Y. Formation of CeO_2-ZrO_2 Solid Solution Nanocages with Controllable Structures via Kirkendall Effect. *J. Am. Chem. Soc.* **2008**, *130*, 2736−2737.

(48) Yang, D.; Kang, X.; Ma, P. a.; Dai, Y.; Hou, Z.; Cheng, Z.; Li, C.; Lin, J. Hollow Structured Upconversion Luminescent $NaYF_4$:Yb^{3+},Er^{3+} Nanospheres for Cell Imaging and Targeted Anti-cancer Drug Delivery. *Biomaterials* **2013**, *34*, 1601−1612.

(49) Wong, H.-T.; Tsang, M.-K.; Chan, C.-F.; Wong, K.-L.; Fei, B.; Hao, J. In vitro Cell Imaging using Multifunctional Small Sized $KGdF_4$:Yb^{3+},Er^{3+} Upconverting Nanoparticles Synthesized by a One-pot Solvothermal Process. *Nanoscale* **2013**, *5*, 3465−3473.

(50) Lee, J.; Park, J. C.; Song, H. A Nanoreactor Framework of a Au@SiO_2 Yolk/shell Structure for Catalytic Reduction of p-Nitrophenol. *Adv. Mater.* **2008**, *20*, 1523−1528.

(51) Lou, X. W.; Li, C. M.; Archer, L. A. Designed Synthesis of Coaxial SnO_2@Carbon Hollow Nanospheres for Highly Reversible Lithium Storage. *Adv. Mater.* **2009**, *21*, 2536−2539.

(52) Boyer, J.-C.; Cuccia, L. A.; Capobianco, J. A. Synthesis of Colloidal Upconverting $NaYF_4$: Er^{3+}/Yb^{3+} and Tm^{3+}/Yb^{3+} Monodisperse Nanocrystals. *Nano Lett.* **2007**, *7*, 847−852.

(53) Boyer, J.-C.; van Veggel, F. C. J. M. Absolute Quantum Yield Measurements of Colloidal $NaYF_4$: Er^{3+}, Yb^{3+} Upconverting Nanoparticles. *Nanoscale* **2010**, *2*, 1417−1419.

(54) Schaefer, H.; Ptacek, P.; Zerzouf, O.; Haase, M. Synthesis and Optical Properties of KYF_4/Yb, Er Nanocrystals, and their Surface Modification with Undoped KYF_4. *Adv. Funct. Mater.* **2008**, *18*, 2913−2918.

(55) Wang, G.; Peng, Q.; Li, Y. Luminescence Tuning of Upconversion Nanocrystals. *Chem.—Eur. J.* **2010**, *16*, 4923−4931.

(56) Zhou, Y.; Yan, B.; He, X.-H. Controlled Synthesis and Up/down-Conversion Luminescence of Self-assembled Hierarchical Architectures of Monoclinic $AgRE(WO_4)_2$:Ln^{3+} (RE = Y, La, Gd, Lu; Ln = Eu, Tb, Sm, Dy, Yb/Er, Yb/Tm). *J. Mater. Chem. C* **2014**, *2*, 848−855.

(57) Suyver, J. F.; Grimm, J.; van Veen, M. K.; Biner, D.; Kramer, K. W.; Gudel, H. U. Upconversion Spectroscopy and Properties of $NaYF_4$ Doped with Er^{3+}, Tm^{3+} and/or Yb^{3+}. *J. Lumin.* **2006**, *117*, 1−12.

(58) Zhao, J.; Jin, D.; Schartner, E. P.; Lu, Y.; Liu, Y.; Zvyagin, A. V.; Zhang, L.; Dawes, J. M.; Xi, P.; Piper, J. A.; Goldys, E. M.; Monro, T. M. Single-Nanocrystal Sensitivity Achieved by Enhanced Upconversion Luminescence. *Nat. Nanotechnol.* **2013**, *8*, 729−734.

(59) Gargas, D. J.; Chan, E. M.; Ostrowski, A. D.; Aloni, S.; Altoe, M. V. P.; Barnard, E. S.; Sanii, B.; Urban, J. J.; Milliron, D. J.; Cohen, B. E.; Schuck, P. J. Engineering Bright Sub-10-nm Upconverting Nanocrystals for Single-molecule Imaging. *Nat. Nanotechnol.* **2014**, *9*, 300−305.

(60) Awang, A.; Ghoshal, S. K.; Sahar, M. R.; Dousti, M. R.; Amjad, R. J.; Nawaz, F. Enhanced Spectroscopic Properties and Judd-Ofelt Parameters of Er-doped Tellurite Glass: Effect of Gold Nanoparticles. *Curr. Appl. Phys.* **2013**, *13*, 1813−1818.

(61) Li, Z.; Wang, L.; Wang, Z.; Liu, X.; Xiong, Y. Modification of $NaYF_4$:Yb,Er@SiO_2 Nanoparticles with Gold Nanocrystals for Tunable Green-to-Red Upconversion Emissions. *J. Phys. Chem. C* **2011**, *115*, 3291−3296.

(62) Liu, N.; Qin, W.; Qin, G.; Jiang, T.; Zhao, D. Highly Plasmon-Enhanced Upconversion Emissions from Au@beta-$NaYF_4$:Yb,Tm Hybrid Nanostructures. *Chem. Commun.* **2011**, *47*, 7671−7673.

(63) Wang, X.; Wang, C.; Cheng, L.; Lee, S.-T.; Liu, Z. Noble Metal Coated Single-Walled Carbon Nanotubes for Applications in Surface Enhanced Raman Scattering Imaging and Photothermal Therapy. *J. Am. Chem. Soc.* **2012**, *134*, 7414−7422.

(64) Moreira, C. S.; Lima, A. M. N.; Neff, H.; Thirstrup, C. Temperature-dependent Sensitivity of Surface Plasmon Resonance Sensors at the Gold-water Interface. *Sensors Actuators, B: Chem.* **2008**, *134*, 854−862.

(65) Qian, H.; Zhu, M.; Wu, Z.; Jin, R. Quantum Sized Gold Nanoclusters with Atomic Precision. *Acc. Chem. Res.* **2012**, *45*, 1470−1479.

(66) Dai, Y.; Xiao, H.; Liu, J.; Yuan, Q.; Ma, P. a.; Yang, D.; Li, C.; Cheng, Z.; Hou, Z.; Yang, P.; Lin, J. In vivo Multimodality Imaging and Cancer Therapy by Near-infrared Light-triggered Trans-platinum pro-drug-conjugated Upconverison Nanoparticles. *J. Am. Chem. Soc.* **2013**, *135*, 18920−18929.

(67) Yang, G.; Gai, S.; Qu, F.; Yang, P. SiO_2@YBO_3:Eu^{3+} Hollow Mesoporous Spheres for Drug Delivery Vehicle. *ACS Appl. Mater. Interfaces* **2013**, *5*, 5788−5796.

(68) Sherlock, S. P.; Tabakman, S. M.; Xie, L.; Dai, H. Photothermally Enhanced Drug Delivery by Ultrasmall Multifunctional FeCo/Graphitic Shell Nanocrystals. *ACS Nano* **2011**, *5*, 1505−1512.

(69) Yu, M.; Li, F.; Chen, Z.; Hu, H.; Zhan, C.; Yang, H.; Huang, C. Laser Scanning Up-conversion Luminescence Microscopy for Imaging Cells Labeled with Rare-earth Nanophosphors. *Anal. Chem.* **2009**, *81*, 930−935.

(70) Kim, T.; Momin, E.; Choi, J.; Yuan, K.; Zaidi, H.; Kim, J.; Park, M.; Lee, N.; McMahon, M. T.; Quinones-Hinojosa, A.; Bulte, J. W. M.; Hyeon, T.; Gilad, A. A. Mesoporous Silica-coated Hollow Manganese Oxide Nanoparticles as Positive T-1 Contrast Agents for Labeling and MRI Tracking of Adipose-derived Mesenchyrnal Stem Cells. *J. Am. Chem. Soc.* **2011**, *133*, 2955−2961.